



Acid-etched Halloysite nanotubes as superior carriers for ciprofloxacin

Ofer Prinz Setter^a, Lisa Dahan^a, Hanan Abu Hamad^a, Ester Segal^{a,b,*}

^a Department of Biotechnology and Food Engineering, Technion – Israel Institute of Technology, Technion City, 3200003, Haifa, Israel

^b The Russel Berrie Nanotechnology Institute, Technion – Israel Institute of Technology, Technion City, 3200003, Haifa, Israel

ARTICLE INFO

Keywords:

Halloysite
Etching
Antibiotic
Ciprofloxacin
Bacteria
E. coli
Loading
Drug delivery
Sustained release

ABSTRACT

Clay minerals have opened new avenues in drug delivery, including antimicrobials, greatly enhancing the stability and efficacy of the active payloads. Among these clay mineral hosts, Halloysite nanotubes (HNT) have emerged as a prominent carrier owing to their intrinsic mesoporous tubular nanostructure and high adsorption capacity. The acidic etching of HNT increases their specific surface area and porosity, consequently enhancing their loading potential. In this work, we show for the first time, that etched HNT (E-HNT) are superior carriers of the potent antibiotic ciprofloxacin (CIP) compared to pristine HNT in terms of loading capacity and antibacterial effect. The loading conditions are optimized within near-physiological conditions to enable future combinations with biomolecules; where CIP loading and release are characterized by UV–Vis measurements and thermogravimetry. Solid-state characterization suggests an adsorptive loading mechanism, involving electrostatic attraction and possible tautomerism. Release experiments show that the loaded CIP exhibits a sustained release profile and maintains its antibacterial potency as confirmed by the broth microdilution (BMD) and zone of inhibition methods. Thus, the facile etching of HNT enhances the nanoclay properties rendering it suitable for future application in drug delivery formulations.

1. Introduction

Clay minerals have gradually conquered a new niche in the world of drug delivery as they present prominent advantages due to their abundancy, intrinsic porosity, and superior adsorption capabilities (Morales et al., 2017; Massaro et al., 2018b; Peña-Parás et al., 2019; Khatoon et al., 2020; Yang and Wang, 2022); while among the nanoclays family, Halloysite nanotubes (HNT) have gained a profound interest over the past two decades. These 600–900-nm long tubular nanoclays are identified as 1:1 aluminosilicates with an intercalated water monolayer ($\text{Al}_2\text{Si}_2\text{O}_5(\text{OH})_4 \cdot n\text{H}_2\text{O}$) (Joussein, 2016). HNT exhibit a mesoporous inner lumen (diameter of ca. 15 nm) (Joussein, 2016) which is ideal for sustained release via hindered out-diffusion, and their substantial silica and alumina specific surface area ($50\text{--}60 \text{ m}^2\text{g}^{-1}$) (Yang et al., 2016) enables ion-exchange and electrostatic interactions with guest molecules (Lvov et al., 2016). In terms of biocompatibility, accumulating data suggest toxicity levels that are comparable with other high aspect ratio nanomaterials (Prinz Setter and Segal, 2020; Rozhina

et al., 2021). Due to their advantageous properties, HNT have been utilized for numerous applications including catalysis (Xiong et al., 2021), energy harvesting (Zhao et al., 2018), and environmental remediation (Wei et al., 2019). Yet, their most prominent application is as carriers for bioactive materials, such as dietary supplements (Blagojević et al., 2022), essential oils (Krepker et al., 2017, 2018), and pesticides (Qin et al., 2022).

It was not until two decades ago, that HNT's unique tubular nanomorphology had been fully elucidated, and a surge of interest arose in utilizing them as nanocarriers for pharmaceuticals. Various small-molecule drugs and macromolecules either charged, polar or hydrophobic have been successfully loaded onto HNT and exhibited a sustained release profile. These range from anti-cancer drugs (Karewicz et al., 2021), through anti-inflammatory drugs (Tan et al., 2014) to bone regeneration factors (Huang et al., 2019) and genetic therapy agents (Massaro et al., 2019). HNT loading process is mostly straightforward, involving their mixing with a concentrated solution of the target drug followed by several vacuuming cycles, centrifugation, washing and

Abbreviations: HNT, Halloysite nanotubes; E-HNT, Acidic-etched HNT; CIP, Ciprofloxacin; BMD, Broth microdilution; FTIR, Fourier transform-infrared; ATR-FTIR, Attenuated total reflectance FTIR; TGA, Thermogravimetric analysis; TEM, Transmission electron microscopy; *E. coli*, *Escherichia coli*; HR-SEM, High-resolution scanning electron microscopy; EDX, Energy-dispersive X-ray; XRD, X-ray diffraction; PBS, Phosphate saline buffer; $\text{O.D}_{600 \text{ nm}}$, Optical density at 600 nm; DTG, Derivative thermogram.

* Corresponding author at: Department of Biotechnology and Food Engineering, Technion – Israel Institute of Technology, Technion City, 3200003, Haifa, Israel.

E-mail addresses: oferp@campus.technion.ac.il (O. Prinz Setter), bouazizlisa@campus.technion.ac.il (L. Dahan), esegal@technion.ac.il (E. Segal).

<https://doi.org/10.1016/j.clay.2022.106629>

Received 28 December 2021; Received in revised form 22 June 2022; Accepted 25 June 2022

Available online 6 July 2022

0169-1317/© 2022 Elsevier B.V. All rights reserved.

drying (Lvov et al., 2016; Santos et al., 2018; Satish et al., 2019; Prinz Setter and Segal, 2020). Loading of many antibiotics (such as oxytetracycline, gentamicin, ciprofloxacin, vancomycin, and metronidazole) has been investigated in an effort to enhance their efficacy and stability (Stavitskaya et al., 2019). Various physiochemical modifications have been proposed to enhance HNT delivery performance including calcination (Deng et al., 2019), polymer or surfactant coating (Tharmavaram et al., 2018), and covalent modifications (Massaro et al., 2017). Among these, acidic etching is one of the most simple and robust routes to increase the specific surface area of HNT and their porosity for improved loading efficiency (Abdullayev et al., 2012; Tharmavaram et al., 2018; Jauković et al., 2021). During the etching process, hydrogen ions solubilize the alumina fraction of HNT, leaving behind only porous amorphous silica while maintaining the rod-like nanostructure (Abdullayev et al., 2012).

Ciprofloxacin (CIP), a potent antibiotic of the fluoroquinolone family, is recognized globally as one of the most used broad-spectrum antibiotics for both humans and animals (Maged et al., 2020). Its mode of action relies on the inhibition of enzymes involved in DNA replication, stopping DNA and protein synthesis (Wolfson and Hooper, 1985). The positively-charged amine groups of CIP and the negatively-charged carboxylic acid group impart the compound a pI of 7.42 – resulting in poor aqueous solubility at physiological pH (Jiang et al., 2016). Thus, CIP has a relatively low bioavailability, that together with its short half-life (Hanna and Saad, 2019) call for more sophisticated dosage forms including drug encapsulation for protection upon degradation and prolonged release. CIP is readily adsorbed by a variety of materials including clay minerals (Duan et al., 2018; Maged et al., 2020; Igwegbe et al., 2021) amidst which HNT have demonstrated superior adsorption capacity (Duan et al., 2018) with reported loaded content of between 2–3 wt. % (Jiang et al., 2016; Duan et al., 2018; Massaro et al., 2021). HNT ability to adsorb CIP is associated with a combination of electrostatic interaction and ion-exchange surface interactions (Duan et al., 2018). The pH range of 6–9 was found to be ideal for CIP adsorption by HNT as CIP is at its zwitterionic state under these conditions (Duan et al., 2018). In addition to pristine HNT, aminosilanized HNT have been reported to strongly interact with CIP via electrostatic attraction overcoming the unwanted complexation of CIP with iron (Rawtani et al., 2017).

Nonetheless, to the best of our knowledge, no attempts have yet been made to investigate the loading of CIP onto acidic-etched HNT (E-HNT). In this report, we present for the first time the advantages of E-HNT over pristine HNT as carriers for CIP. Loading conditions were optimized within a restricted physiological range (phosphate buffer saline, pH 6–7) to enable the future combination of the proposed protocol with any biofunctionalization of the E-HNT. The loaded clay minerals were analyzed by a series of solid-state characterization techniques, including Fourier transform-infrared (FTIR) spectroscopy, thermogravimetric analysis (TGA), and transmission electron microscopy (TEM). Lastly, the release profile of the loaded CIP was obtained, and its exerted antibacterial activity was investigated against *Escherichia coli* (*E. coli*) by the broth microdilution (BMD) method in combination with zone of inhibition measurements.

2. Materials and methods

2.1. Chemicals and materials

Halloysite nanotubes were purchased from NaturalNano, USA (mined at the Atlas Mining Dragon Mine in Utah, USA), and dried at 150 °C for 3 h. Concentrated sulfuric acid was obtained from Sigma-Aldrich Chemicals (Israel). Phosphate buffer saline (PBS) pH 7.2 0.1 M was prepared using Milli-Q water (18 MΩ-cm) mixed with 50 mM sodium hydrogen phosphate (Merck, Germany), 17 mM sodium dihydrogen phosphate monohydrate (Merck, Germany), and 68 mM sodium chloride (BioLab, Israel). All solutions were passed through a

0.22 μm membrane filter before use. Ciprofloxacin was supplied by Sigma-Aldrich Chemicals (Israel), and acetic acid was purchased from Gadot Group (Israel). *E. coli* K-12 was generously provided by Prof. Sima Yaron (Technion) and cultured in Luria broth (LB) medium containing 10 g L⁻¹ Bacto™ Tryptone (BD, USA), 5 g L⁻¹ Bacto™ yeast extract (BD), and 5 g L⁻¹ sodium chloride. LB agar plates for culturing were prepared by adding 17 g L⁻¹ Bacto™ agar (BD, USA) to the LB medium.

2.2. Acid etching of HNT

HNT acidic etching was performed as previously reported (Barfod et al., 2020). Briefly, an aqueous suspension of 0.15 mg HNT mL⁻¹ was subjected to cycles of 20-min vacuuming restoring atmospheric pressure after each cycle. Next, the suspension was acidified with sulfuric acid at a final concentration of 17 vol. % and mixed at 105–110 °C for 16 h. After the reaction, 400 mL of water were added to the mixture and the E-HNT were separated by filtration and washed again with water. Finally, the resulting E-HNT were dried at 120 °C for 2 h.

2.3. Ciprofloxacin loading

The loading procedure was based on previous works (Rawtani et al., 2017) and included the optimization of three main parameters: (1) CIP concentration, (2) HNT concentration, and (3) loading duration (see scheme in Fig. 2). First, a stock suspension of E-HNT was prepared by sonicating 33 mg mL⁻¹ of clay mineral in PBS using a Vibra-Cell ultrasonic probe equipped with a microtip, (Sonics & Materials Inc. USA). A concentrated stock solution of CIP was prepared by solubilizing 620 μg mL⁻¹ in PBS acidified to pH 5.1 with acetic acid. Then, E-HNT stock and concentrated CIP stock solutions were combined to prepare the mixtures detailed in Table 1 in triplicates. Each mixture was shaken for 15 min at 1500 rpm by a thermoshaker for microtubes (MRC, Israel) and then evacuated at 100 mbar to ensure complete filling of E-HNT pores (Lisuzzo et al., 2019a, 2019b; Massaro et al., 2021) for three cycles to the total loading durations detailed in Table 1.

After each vacuum cycle, atmospheric pressure was restored. The loaded E-HNT were separated by centrifugation at 9167 x g centrifugation force and washed with PBS following a second round of centrifugation. All supernatant solutions were collected and measured for absorbance at 272 nm (Rawtani et al., 2017) using a quartz 96-well plate and a microplate reader (Varioskan Flash, Thermo Fisher Scientific, USA). Fig. S1 (Supporting Information) presents a characteristic calibration curve for CIP quantification. The CIP loaded content (wt. %) and the loading efficiency were calculated according to Eq. (1) and Eq. (2), respectively.

$$\text{CIP loaded content} = \frac{m_{\text{CIP}} - (m_{\text{after loading}} + m_{\text{wash}})}{m_{\text{E-HNTs}}} \bullet 100 \quad (1)$$

$$\text{Loading efficiency} = \frac{m_{\text{CIP}} - (m_{\text{after loading}} + m_{\text{wash}})}{m_{\text{CIP}}} \bullet 100 \quad (2)$$

where m_{CIP} stands for the CIP mass (μg) in the control loading solution (no HNT), $m_{\text{after loading}}$ and m_{wash} are the CIP mass in the supernatant after the first and second centrifugations, respectively, and $m_{\text{E-HNTs}}$ represents E-HNT mass of in the loading mixture.

Following each loading experiment, the pellets were dried in a vacuum oven at 90 °C overnight and stored in a desiccator. In addition, pristine HNT (not subjected to etching) were also loaded under the same conditions. Control samples without CIP were prepared both for E-HNT and HNT by repeating the loading protocol without the addition of CIP.

2.4. Sedimentation

The sedimentation rate of the different clay mineral suspensions was visually monitored in a cuvette (1 mL) under the optimal loading

Table 1
Mixture compositions for CIP loading optimization.

HNT concentration (mg mL ⁻¹)	4				10			
CIP concentration (μg mL ⁻¹)	80	160	320	160	320	420		
Loading duration (min)	45	180	90	180	90	180	90	180

conditions. As a negative control, pristine HNT and E-HNT were also suspended by the same procedure excluding the CIP.

2.5. Infrared spectroscopy

The interactions between the loaded CIP and its clay mineral hosts were investigated by attenuated total reflectance (ATR) FTIR spectroscopy using a Thermo 6700 FT-IR spectrometer (USA) equipped with a Smart iTR diamond ATR device. All spectra of loaded clay mineral were normalized to the highest band around 1000–1030 cm⁻¹ attributed to Si-O bonds (Yuan et al., 2008; Sun et al., 2015) which is not expected to be affected by the loading procedure.

2.6. Thermogravimetric analysis (TGA)

TGA was performed by a TGAQ5000 instrument (TA Instruments, USA). The dynamic high-resolution mode was used (Sensitivity number: 1; Resolution: 6) at a heating rate of 5 °C min⁻¹ up to 580 °C. Results were processed by Universal Analysis 200 version 4.5A build 4.5.0.5 software. Each sample was analyzed in triplicate. TGA data are normalized to sample weight at 100 °C to be expressed on a dry basis. The loaded CIP (wt. %) content was determined according to Eq. (3).

$$CIP \text{ loaded content (wt. \%)} = \frac{R_{neat} - R_{loaded}}{100 - R_{CIP}} \cdot 100 \quad (3)$$

where R_{neat} is the residue of the control neat sample (E-HNT or HNT) at 580 °C (wt. %), R_{loaded} represents the residue of loaded sample (E-HNT or HNT) at 580 °C (wt. %), and R_{CIP} is the residue of pure CIP at 580 °C (wt. %).

2.7. Scanning electron microscopy

Dry samples were imaged using Carl Zeiss Ultra Plus (Germany) high-resolution scanning electron microscope (HR-SEM) at an accelerating voltage of 1.3 keV and a working distance of 3 mm.

2.8. X-ray diffraction (XRD)

XRD patterns were measured by a Rigaku X-ray diffractometer (SmartLab, Rigaku, Tokyo, Japan), at 2θ values from 5 ° to 90 ° and a rate of 2 ° min⁻¹. The CuKα radiation source power was 40 kV, and current was set to 30 mA.

2.9. Transmission electron microscopy and energy dispersive X-ray spectroscopy

The drop cast method was used to prepare the different samples for imaging on carbon type-B grids. Imaging was performed by an FEI Tecnai G2 T20 S-Twin transmission electron microscope (TEM) coupled with an energy-dispersive X-ray (EDX) detector at an accelerating voltage of 200 keV. EDX data were processed by TIA (TEM Imaging & Analysis) software version 4.12, FEI Company, OR, USA.

2.10. Antibacterial activity by the zone of inhibition technique

The antibacterial activity of loaded E-HNT and loaded pristine HNT was also investigated using the zone of inhibition technique. 20 mg of each sample were pressed into a round disk under 10 MPa using a

manual tableting press (76YP-15A, MRC Lab, China) equipped with a 7 mm die. Three disks were prepared and tested for each sample. A fresh *E. coli* K-12 culture in LB medium was prepared from a single colony incubated at 37 °C overnight. The culture was diluted to 10⁵ CFU mL⁻¹ and spread on an LB agar petri dish on the center of which one disk was positioned. After overnight incubation at 37 °C, the inhibition zone diameters were measured and divided by the petri dish diameter (90 mm) to calculate the percentage of inhibition. For negative control, we used disks made of E-HNT and pristine HNT without CIP. A positive control comprised a filter paper disk with a diameter of 7 mm loaded with 390 μg of CIP (equivalent to the average potency of disks tableted from loaded E-HNT and pristine HNT).

2.11. Ciprofloxacin release studies

The release profile of loaded CIP was obtained by using 6-well Corning® Transwell® polycarbonate membrane inserts (Corning, USA), with a 0.45 μm pore diameter. About 2 mg of loaded clay mineral (E-HNT or pristine HNT) were accurately weighted onto the upper side of the insert, and then the insert was submerged in a well filled with 2.8 mL of PBS. Then, 1.2 mL PBS were inserted on top of the insert, and the plate was gently shaken at 200 rpm. Aliquots were taken from the bottom liquid at 1-h intervals. Each aliquot was taken from a separate well, and the absorbance of each aliquot was measured at 272 nm for CIP quantification. The diffusion rate of CIP through the insert membrane was studied by adding pure CIP solution on top of the insert instead of the loaded clay minerals.

An exponential saturation model was fitted for CIP release profiles. Models were fitted using Prism software (version 9.2 (3320), GraphPad Software LLC) according to Eq. (4):

$$R(t) = R_s - (R_s - R_0) \cdot e^{-kt} \quad (4)$$

where t is the time (h), $R(t)$ is the accumulative release of CIP at time t (% accumulative release), R_s stands for the plateau value of CIP accumulative release at infinite time (% accumulative release), R_0 stands for the accumulative release at time 0 (constrained as 0), and k is the rate constant (h⁻¹) and is constrained as >0.

2.12. Time-resolved antibacterial activity

The antibacterial activity of each interval from the release experiment was studied by the BMD method. A fresh culture of *E. coli* K-12 in LB medium was prepared from a single colony by overnight incubation at 37 °C. To revive the bacteria into their logarithmic growth stage, a decimal dilution of the culture was incubated for additional 2 h at 37 °C. In a 96-well plate, binary dilutions of the released CIP aliquots were mixed with the revived *E. coli* to a final optical density (O.D_{600 nm}) of 0.1. Bacteria growth was monitored by periodic O.D_{600 nm} measurements using a microplate reader at 37 °C incubation under gentle shaking for 10 h. Normalized growth inhibition was calculated according to Eq. (5).

$$NI = \frac{OD_{600 \text{ nm } E. coli} - OD_{600 \text{ nm } t}}{OD_{600 \text{ nm } E. coli}} \cdot \frac{1}{C} \quad (5)$$

where NI stands for the normalized inhibition (mg⁻¹ mL), $OD_{600 \text{ nm } E. coli}$ represents the optical density at 600 nm measured after 10 h of incubation at 37 °C for *E. coli* culture, $OD_{600 \text{ nm } t}$ represents the optical density at 600 nm measured after 10 h of incubation at 37 °C for *E. coli* culture containing an aliquot taken from the release experiment at time t , and C

is the clay mineral concentration in the release experiment (mg mL^{-1}). Note that to achieve adequate selectivity below the minimal inhibitory concentration, a dilution of 1:32 of the release aliquots was used for the calculation.

An exponential saturation model was fitted for the normalized growth inhibition measured for the aliquots from the release experiments. Models were fitted using the Prism software (version 9.2 (3320), GraphPad Software LLC) according to Eq. (6):

$$NI(t) = NI_s - (NI_s - NI_{t0}) \bullet e^{-kt} \tag{6}$$

where $NI(t)$ is the normalized inhibition for release time t ($\text{mg}^{-1} \text{mL}$), NI_s stands for the plateau value of normalized growth inhibition at infinite time ($\text{mg}^{-1} \text{mL}$), NI_{t0} is the normalized growth inhibition at time 0 (constrained as 0), and k is the rate constant (h^{-1}) which is constrained as >0 .

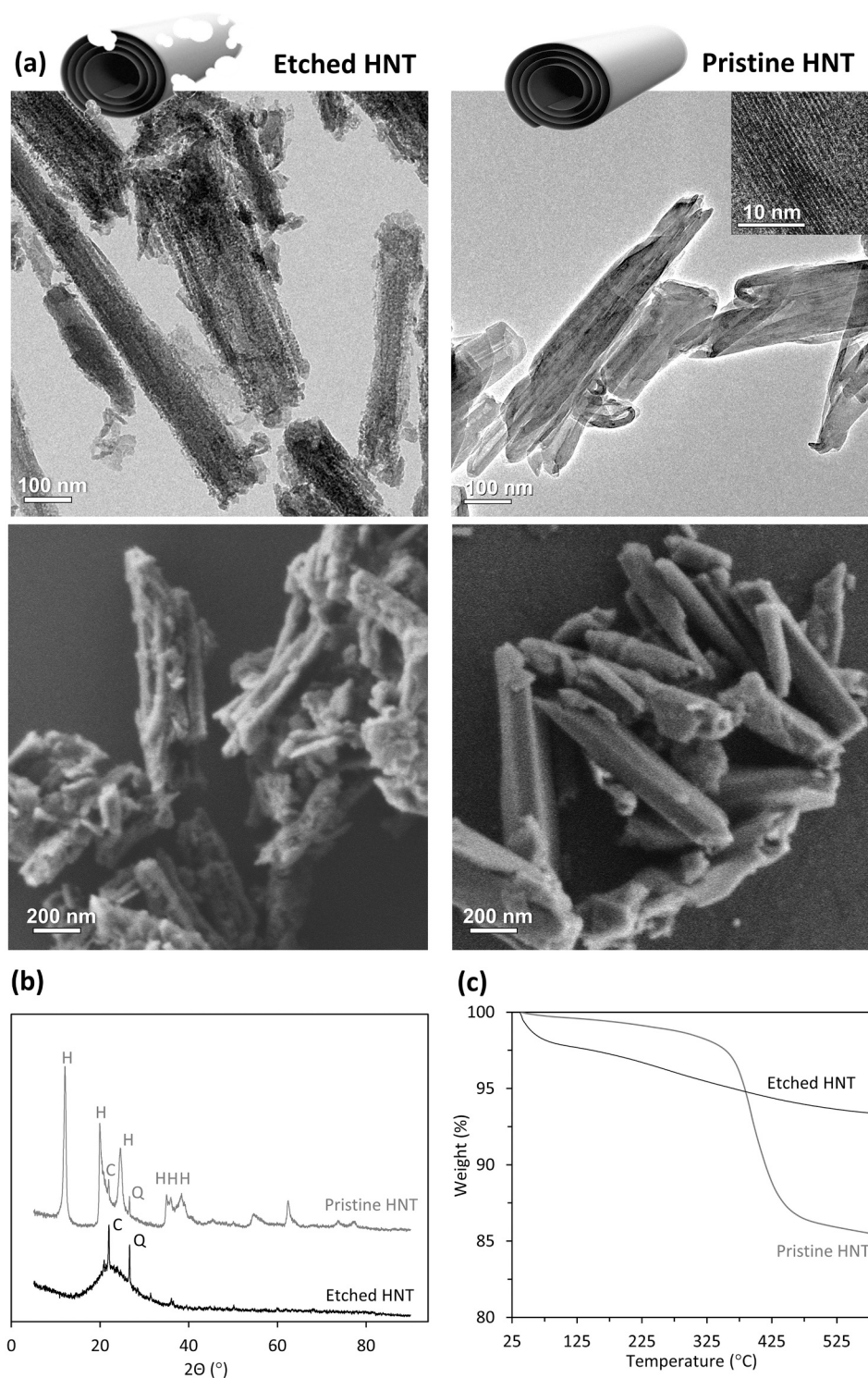


Fig. 1. Characterization of pristine and etched HNT: (a) Electron micrographs of etched HNT (left) and pristine HNT (right) taken by TEM (upper panel, inset presents a high magnification image) and SEM (lower panel); (b) X-ray diffractograms of etched and pristine HNT. C – cristobalite, Q – quartz (Pasbakhsh et al., 2013); (c) High-resolution thermograms of etched and pristine HNT.

3. Results and discussion

3.1. Acidic etching

Pristine HNT were exposed to acidic conditions and the nanostructure of the resulting etched HNT (termed as E-HNT) was characterized by electron microscopy. The E-HNT exhibit a more coarsened surface in comparison to pristine HNT while their rod-like morphology is maintained, see Fig. 1a and also Fig. S2 (Supporting Information) for additional SEM micrographs. Yet, the characteristic 7-Å interlayer space of the pristine HNT (Joussein et al., 2005; Abdullayev and Lvov, 2016), calculated using the inset of Fig. 1a (see Supporting Information, Fig. S3), is observed to be lost following the etching process. The latter is ascribed to the selective etching of the HNT alumina layers leaving nanometric crevices of amorphous silica, which in turn greatly increased the specific surface area from 25.6 to 128 m² g⁻¹, as measured by nitrogen adsorption (Barfod et al., 2020) (See Table S1, Supporting Information, for a detailed summary of the physicochemical characterization of pristine HNT and E-HNT). Moreover, the XRD pattern of the E-HNT presented in Fig. 1b shows an amorphous halo; whereas, the pattern of pristine HNT depicts main peaks at 2θ = 12, 20, 25, 35, 36 and 38°. These are associated with tubular HNT characteristic d-spacing: 7.4 Å (001), 4.4 Å (020), 3.6 Å (002), 2.56 Å (130), 2.5 Å (131) and 2.4 Å (003), respectively (Joussein et al., 2005; Abdullayev et al., 2012; Pاسبakhsh et al., 2013). This difference in the XRD patterns suggests the loss of the layered structure of the HNT during the etching process. Trace amounts of quartz and cristobalite impurities are also observed in the diffractograms of both etched and pristine HNT.

Thermogravimetric analysis results of E-HNT, shown in Fig. 1c, reveal a weight loss of about 2.5 wt. % up to 150 °C which is ascribed to the loss of adsorbed moisture (Yuan et al., 2008; Zhao et al., 2015; Prinz Setter et al., 2021), where for pristine HNT only a minor weight loss (~0.5 wt. %) is observed. Thus, the 5-fold increase in adsorbed moisture content in E-HNT may be attributed to their higher surface area in comparison to pristine HNT (Table S1, Supporting Information). No intercalated water is expected to be present in the HNT used in this work due to their irreversible anhydrous 7-Å state (Joussein et al., 2005) indicated by both high-resolution TEM and XRD measurements (Fig. 1a and b, respectively). At higher temperatures, pristine HNT show a

characteristic mass loss at 400 to 500 °C associated with the dehydroxylation of aluminol groups (Yuan et al., 2008; Daou et al., 2020), whereas E-HNT do not exhibit this thermal decomposition event, providing additional evidence for the acidic etching of the alumina (Prinz Setter et al., 2021). This finding is further supported by the EDX spectrum of the E-HNT (Fig. S4, Supporting Information), revealing an Al : Si ratio of 0.02, much lower than the characteristic Al : Si ratio of pristine HNT (≥1) (Yang et al., 2016; Barfod et al., 2020).

3.2. Ciprofloxacin loading

The loading of E-HNT with CIP was investigated at varying loading durations and concentrations of CIP or E-HNT, as illustrated in Fig. 2.

CIP loading was firstly investigated by quantitating CIP concentration before and after the loading using UV absorbance measurements at 272 nm (for a characteristic calibration curve see Fig. S1 in the Supporting Information). Fig. 3a and b summarize the wt. % of loaded CIP obtained under the different loading conditions as well as the CIP loading efficiency calculated according to Eq. (1) and Eq. (2), respectively. The lowest concentration of CIP solution (80 µg mL⁻¹), did not yield any substantial loading after 45 min; while extending the loading duration to 180 min has slightly improved the loading to 0.18 wt. % see Fig. 3a (left panel). Lowering the loading duration to 90 min did not impair CIP loading, regardless of neither CIP nor HNT concentration. For E-HNT concentration of 4 mg mL⁻¹, increasing CIP concentration from 80 through 160 to 320 µg mL⁻¹ resulted in an increased loaded CIP content (0.2, 0.9, and 1.8 wt. %, respectively). Yet, the achieved loading efficiency (Fig. 3b, left panel) did not follow this trend, reaching a saturation of ~20 % already at a CIP loading concentration of 160 µg mL⁻¹. To improve the loading efficiency, we increased the E-HNT concentration from 4 to 10 mg mL⁻¹, increasing the loading efficiency to 40% and 55% at CIP concentrations of 160 and 420 µg mL⁻¹, respectively (Fig. 3b right panel). This trend was also observed for loaded CIP content (up to 2.3 wt. % at 420 µg CIP mL⁻¹, see Fig. 3a right panel). As a further increase in CIP loading concentration could not be achieved due to the CIP solubility limitation (Ross and Riley, 1990), the optimal loading conditions for E-HNT were set as 10 mg mL⁻¹ E-HNT in a solution of 420 µg mL⁻¹ CIP for 90 min. Loading the pristine HNT (not etched) under the same conditions resulted in inferior CIP loading, 40% lower than that

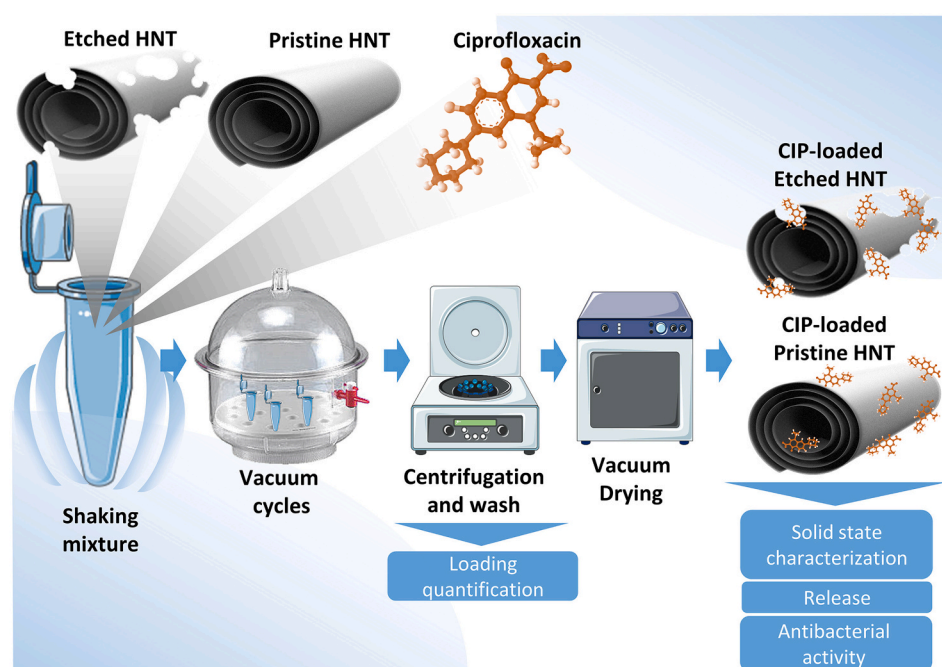


Fig. 2. A scheme illustrating the loading procedure of etched and pristine HNT with CIP. Mixtures of the clay mineral and antibiotic at varying concentrations are shaken and subjected to vacuum for different loading durations. The mixtures are then centrifuged, washed, and dried under vacuum. UV measurements of the supernatants enable the quantification of CIP loading. The dry powders are investigated for their physicochemical properties as well as their CIP release profiles. In addition, the antibacterial activity of the released CIP is studied.

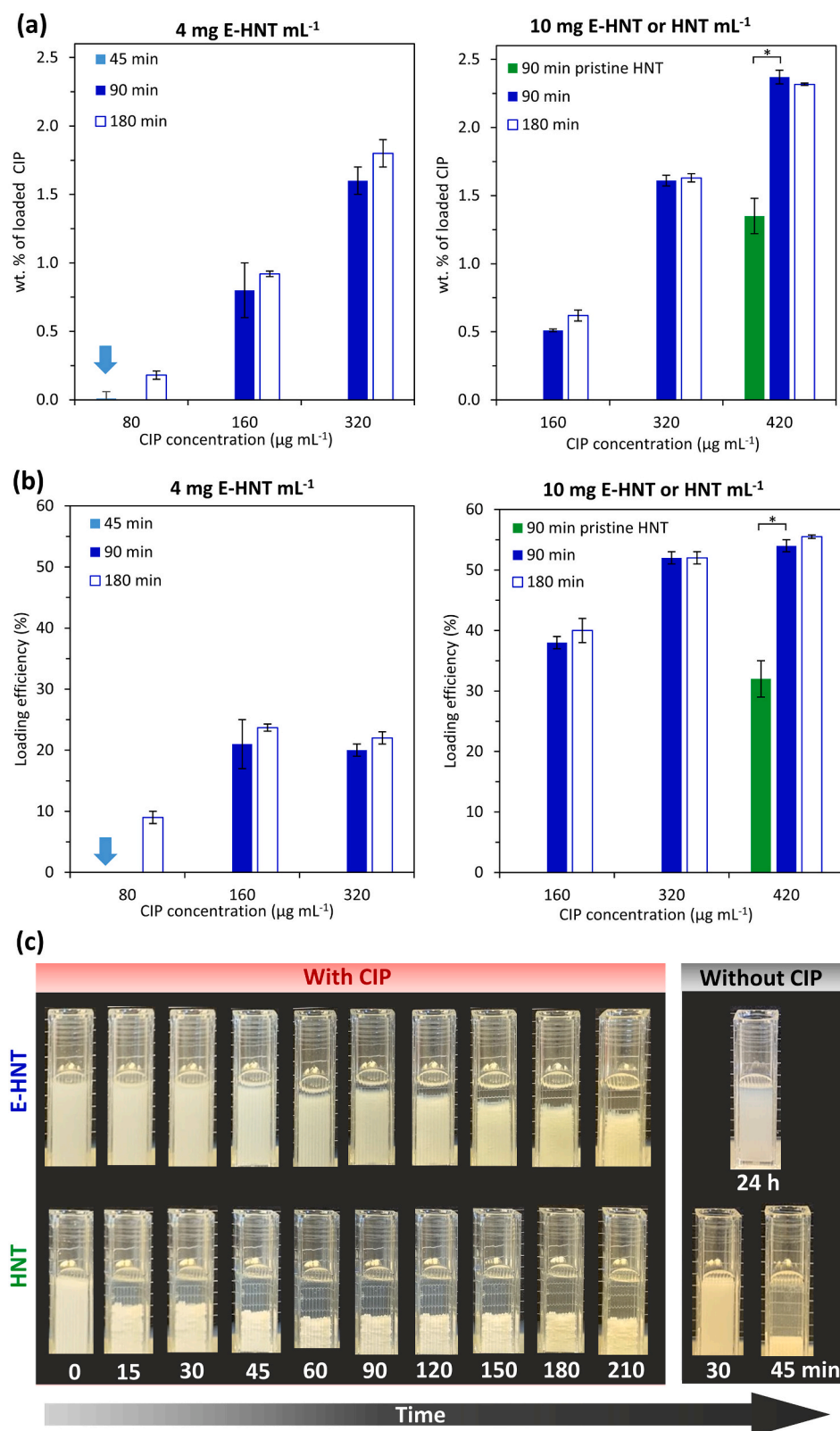


Fig. 3. Comparison of CIP loading to etched HNT (E-HNT) and pristine HNT. (a) wt. % of loaded CIP and (b) loading efficiency for E-HNT (blue bars) and pristine HNT (green) under different loading conditions: loading duration (45 min – light blue arrow, 90 min – dark blue, 180 min – white), and clay mineral concentration (4 mg mL⁻¹ – left panel, 10 mg mL⁻¹ – right panel). Error bars represent SD, $n = 3$, and * indicates $p < 0.01$, two-tail t -test. (c) Time-resolved visual observation of E-HNT (upper panel) and pristine HNT (lower panel) suspensions w/ and w/o CIP. (For interpretation of the references to colour in this figure legend, the reader is referred to the web version of this article.)

achieved for E-HNT (Fig. 3a and b). Our results fall in the range of previously reported values for CIP-loaded pristine HNT (2–3%) (Jiang et al., 2016; Duan et al., 2018; Massaro et al., 2021). It should be pointed out the variability between the achieved loading values may arise from the differences in loading techniques, HNT geological origin, and CIP polymorph, as detailed in Table S2 (Supporting Information).

As E-HNT exhibit a 5-fold higher specific surface area than pristine HNT (Barfod et al., 2020), their higher loading suggests an improved adsorptive loading mechanism, as previously proposed for pristine HNT (Jiang et al., 2016) and other clay minerals (Duan et al., 2018; Maged et al., 2020). Moreover, we visually observed that the sedimentation rate of the clay mineral increased in the presence of CIP as depicted in

Fig. 3c, and pristine HNT sedimented more rapidly in comparison to the etched ones. Suspension stability is highly sensitive to changes in the HNT (Lisuzzo et al., 2019a, 2019b) and as such, faster sedimentation can be ascribed to the adsorption of CIP molecules onto HNT surface (Zhao and Liu, 2008). The superior suspension stability of E-HNT in an aqueous medium can be attributed to their smaller size (Fig. S5, Supporting Information), and higher hydrophilicity due to the additional

silanol groups exposed on their surface (Sun et al., 2015; Garcia-Garcia et al., 2017). This significant advantage over pristine HNT may facilitate the adsorptive loading. Further investigation of the CIP - E-HNT interactions is discussed in the next section.

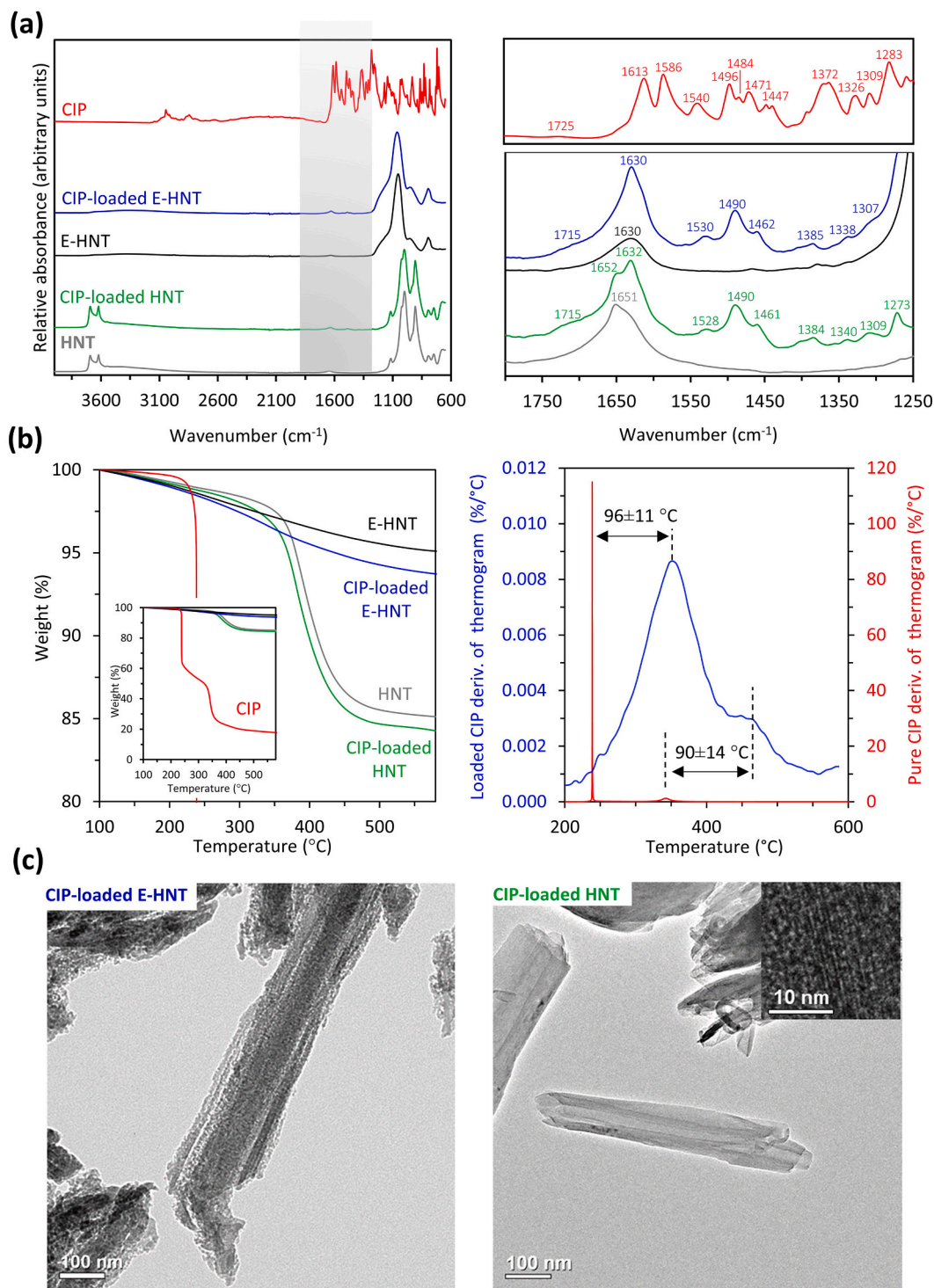


Fig. 4. Solid-state characterization of CIP loading E-HNT and pristine HNT: (a) FTIR-ATR spectra between 4000 and 600 cm^{-1} (left panel) and 1800–1250 cm^{-1} (right panel), note that colors of the spectra are kept consistent throughout; (b) TGA thermograms at a high-resolution mode with a zoom out inset (left) and DTG curves for pure CIP (red) and CIP-loaded E-HNT (blue). Horizontal arrows indicate temperature shifts (average \pm SD, $n = 3$); (c) TEM micrographs with a high magnification inset. (For interpretation of the references to colour in this figure legend, the reader is referred to the web version of this article.)

3.3. Solid-state characterization and loading mechanism

Characterization: To investigate the nature and role of E-HNT - CIP interactions, we characterized their physicochemical properties. Fig. 4a presents the FTIR spectra of both pristine and E-HNT where a sharp band is observed around 1000–1050 cm^{-1} , attributed to Si-O bonds (Yuan et al., 2008; Sun et al., 2015), for the two clay minerals. Conversely, the distinctive bands at 3693 and 3619 cm^{-1} , ascribed to aluminol groups of the pristine HNT (Abdullayev et al., 2012), are not observed for the E-HNT, indicating the high degree of alumina etching. When zooming in to the range of interest (Fig. 4a right panel), pristine and E-HNT depict only a single band due to adsorbed water at 1651 and 1630 cm^{-1} , respectively (Saklar and Yorukoglu, 2015). As for pure CIP, characteristic bands are observed, including bands at 1725, 1613, 1586, 1484, 1372, and 1283 cm^{-1} , and their respective assignments are summarized in Table 2. The spectra of CIP-loaded E-HNT depict three main differences in comparison to the spectrum of pure CIP: (i) a distinct shift of the C=O ketone stretch band (Mesallati et al., 2017) from 1613 cm^{-1} to 1630 cm^{-1} , (ii) diminishing of the bands at 1586 and 1372 cm^{-1} associated with the carboxylate ion asymmetric and symmetric vibrations (Mesallati et al., 2017), respectively, and (iii) a slight rise of the band between 1680–1760 cm^{-1} which is attributed to carbonyl stretch of the unionized carboxylic acid group of CIP (Mesallati et al., 2016). The combination of these differences implies the tautomerism of pure CIP from the zwitterionic to the unionized form upon loading into the clay mineral (Mesallati et al., 2016) and was also reported for the loading of CIP into smectite (Memenfo et al., 2021). Such a transition could arise from possible ion-exchange interactions between the antibiotic and the clay mineral, and may be accounted for the inferior suspension stability of the CIP-loaded clay minerals (see Fig. 3c). Notably, the spectra of both CIP-loaded HNT and CIP-loaded E-HNT display high similarity. In addition to the aforementioned differences, other characteristic CIP bands in the loaded clay mineral spectra depict shifts to both higher and lower wavenumbers (e.g., from 1540 to 1530, 1447 to 1462, and 1326 to 1338 cm^{-1}). Such a behavior was also reported for the loading of CIP HCl onto silver nanoparticles (Mohsen et al., 2020) and acid-treated bentonite (Maged et al., 2020). For the latter, the shifts were associated with various interactions between CIP and the clay mineral surface, including electrostatic forces, hydrogen bonding, and intercalation through cation exchange. Thus, our FTIR results support an adsorptive mechanism for the loading of CIP onto E-HNT, similar to that previously suggested for pristine HNT (Duan et al., 2018). Furthermore, since E-HNT are composed mostly of silica, it could be deduced that adsorbed CIP interacts with pristine HNT also mainly through the latter's silica surface.

The thermal degradation of pure CIP, presented in Fig. 4b left panel, consists of two main events at 238 and 346 °C with a residue of about 20 wt. % at 580 °C, as was previously reported (El-Gamel et al., 2012; He et al., 2015). The loaded clay minerals display lower residues at 580 °C compared to the corresponding neat clay minerals, attributed to the decomposition of the loaded CIP (1.1±0.8 and 1.7±0.3 wt. % for loaded pristine HNT and E-HNT, respectively). The higher CIP loading

Table 2

Interpretation of main bands in CIP FTIR spectrum, see Fig. 4a for respective spectra.

Band (cm^{-1})	Band assignment
1725	Carbonyl stretch of unionized carboxylic acid group*
1613	Carbonyl stretch of ketone*
1584	Asymmetric vibration of carboxylate ion*
1484	Stretching of C–N groups**
1372	Symmetric vibration of carboxylate ion*
1280	O-H deformation vibration***

* Mesallati et al. (2017);

** Massaro et al. (2021);

*** Maged et al. (2020).

measured for the E-HNT by TGA agrees with UV absorbance results (Fig. 3a), favoring E-HNT over pristine HNT in terms of CIP loading. Nonetheless, some differences between the two analytical methods are to be expected.

To better elucidate the loading effect on the thermal stability of CIP, we extracted the derivative thermograms (DTG) of the loaded CIP by subtracting the DTG of neat E-HNT from the DTG of CIP-loaded E-HNT. The obtained DTG plot is presented in Fig. 4b right panel and is compared to that of pure CIP. The loaded CIP is found to degrade in a two-step manner similar to pure CIP; yet, it displays superior thermal stability as the degradation temperatures are observed to increase by 90–95 °C. This stabilizing effect suggests strong intermolecular interactions between the loaded CIP and the E-HNT host (Massaro et al., 2018a; Fakhrollina et al., 2019; Jauković et al., 2021; Memenfo et al., 2021). This analysis could not be performed for the pristine HNT as the aluminol dehydroxylation event overlaps with CIP degradation (see Fig. S6, Supporting Information).

Following CIP loading, no apparent morphological changes were observed for etched and pristine HNT, see Fig. 4c (loaded clay) and Fig. 1a (neat clay without CIP). In addition, the characteristic 7-Å interlayer space of pristine HNT (Joussein et al., 2005; Abdullayev and Lvov, 2016) is also retained after CIP loading (see measurement details in Fig. S3, Supporting Information.). These findings further support an adsorptive mode of interaction between the antibiotic and the clay.

Loading mechanism: At the relevant pH range used (pH 6–7), CIP is expected to be present mainly at its zwitterionic form (Jiang et al., 2016; Cheng et al., 2018), namely its protonated amine residue is positively charged while its deprotonated carboxylic residue is negatively charged. Therefore, electrostatic interactions between the CIP positively-charged amine and the HNT negatively-charged surface are expected to play the main role in the adsorption of CIP onto E-HNT. This is supported by the higher sedimentation rate observed for CIP-loaded E-HNT (Fig. 3c) ascribed to the masking effect of the adsorbed CIP molecules. The same electrostatic interactions were proposed for pristine HNT in many previous reports (Jiang et al., 2016; Cheng et al., 2018; Duan et al., 2018; Wang et al., 2021b), and were recently supported by a computational molecular model (Massaro et al., 2021). Furthermore, FTIR measurements indicate a subsequent tautomerism of the loaded CIP from its original zwitterionic form to a unionized form, see Fig. 4a; the same was also reported for CIP loading onto smectite (Memenfo et al., 2021). Intercalation of CIP into E-HNT is excluded as the E-HNT do not exhibit any interlayer gap (as evidenced by TEM and XRD analyses, see Fig. 1a and b, respectively). Thus, CIP loading onto E-HNT is ascribed to solely surface interactions. Calculating the relative surface coverage of loaded CIP (70 Å² (Jiang et al., 2016)) onto pristine and E-HNT, yields 70 and 26 %, respectively. The decreased coverage of E-HNT may be ascribed to a lesser surface density of sites available for electrostatic interactions or a lower surface charge density possibly due to the elimination of the alumina component (Jenne, 1972).

3.4. CIP antibacterial potency and release

The antibacterial activity of the loaded clay minerals was studied using the inhibition zone method and representative images are depicted in Fig. 5a. After 24 h of incubation, the CIP-loaded E-HNT and pristine HNT exerted an inhibitory effect (57 ± 3 and 53 ± 5 %, respectively) comparable to the positive control containing only CIP (53 ± 1 %), and no significant difference was found between the three treatments ($p > 0.05$). No inhibition of growth was observed for the negative control tablets made of E-HNT or pristine HNT without CIP. Based on these findings it could be concluded that the loaded CIP retains its antibacterial activity and is as effective as pure CIP. This result corresponds with a previous report regarding the superior antibacterial activity of CIP-loaded HNT against *Pseudomonas aeruginosa* also measured by the zone of inhibition method (Lvov et al., 2016; Stavitskaya et al., 2019). To further elucidate the kinetics of CIP release, we

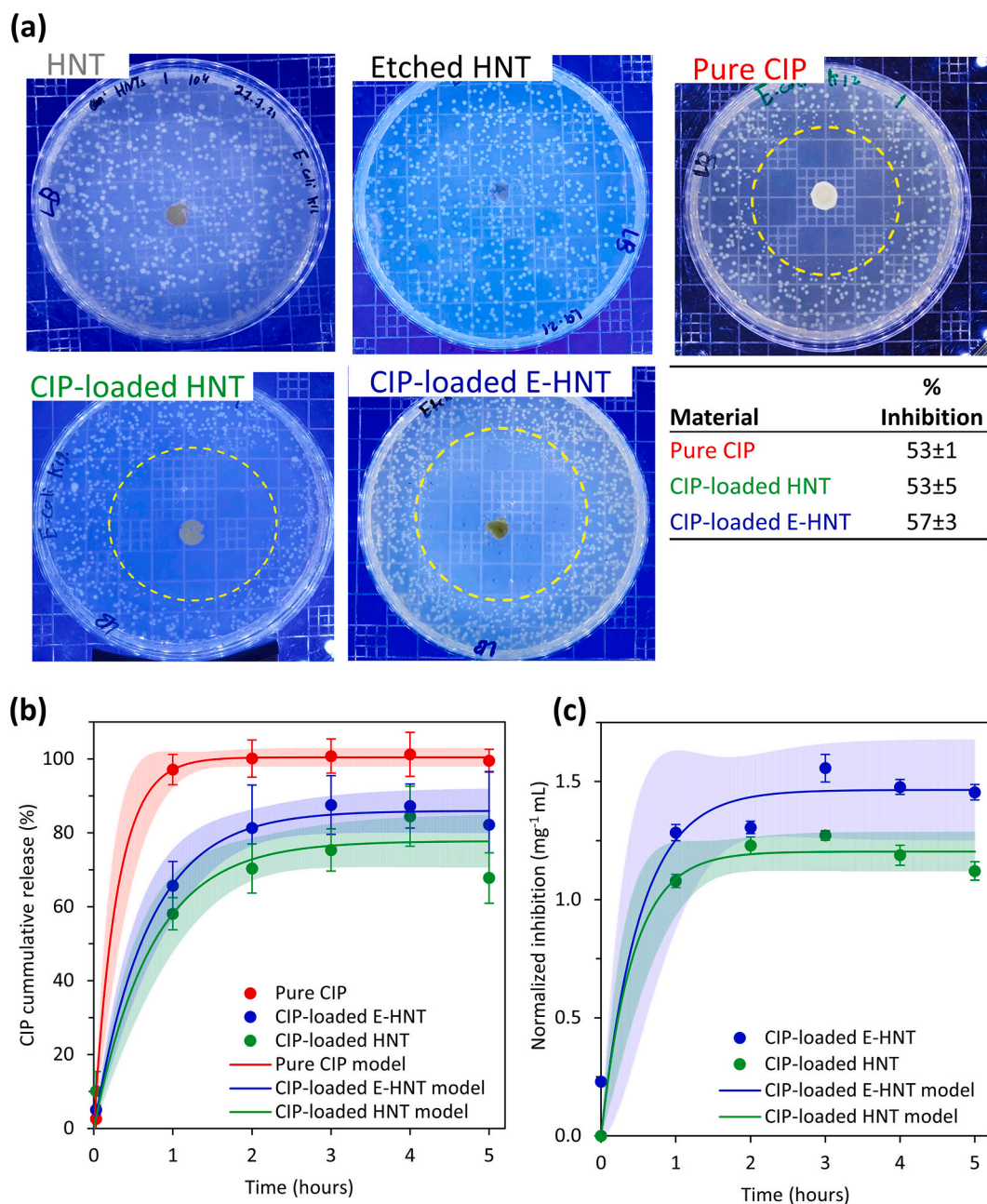


Fig. 5. Antibacterial activity and release profile of CIP from etched and pristine HNT: (a) Zone of inhibition study against *E. coli* K-12. Representative images of petri dishes treated with pristine HNT, E-HNT, CIP-loaded pristine HNT, CIP-loaded E-HNT, and a filter paper disk loaded with CIP amount equivalent to the average of the loaded clay minerals. Bottom right: % inhibition of the different treatments expressed as average \pm SD, $n = 3$. (b) Release profile of CIP-loaded E-HNT (blue) and pristine HNT (green), as well as pure CIP (red). Error bars represent SD ($n = 3$). Solid lines represent a one-phase exponential saturation model, and light areas represent confidence bands at 95% confidence. The model was fitted by Prism software (version 9.2 (3320), GraphPad Software LLC), constraining the time zero value to be zero and the time constant to be positive. (c) Normalized growth inhibition against *E. coli* K-12 as measured by the BMD method for aliquots taken from the release experiment of CIP-loaded E-HNT (blue) and pristine HNT (green). Solid lines represent a one-phase exponential saturation model and light areas represent confidence bands at 95% confidence. The model was fitted by Prism software (version 9.2 (3320), GraphPad Software LLC), constraining the time zero value to be zero and the time constant to be positive. (For interpretation of the references to colour in this figure legend, the reader is referred to the web version of this article.)

quantified the released amount and then studied its antibacterial effect at each time point. The release profiles of CIP from loaded E-HNT or pristine HNT into PBS pH 7.2 were obtained by UV absorbance measurements and are presented in Fig. 5b. The profiles are compared to the diffusion rate of pure CIP solution through the membrane used in these experiments. A one-phase exponential saturation model is fitted for each of the experiments and the obtained R square values are >0.9 . The loaded HNT, whether pristine or etched, exhibit a sustained release profile which is significantly different from the pure CIP profile ($p <$

0.05) with a half-life time of 0.5 h and a plateau value of about 80% cumulative release. No significant difference is observed between the release profiles of the two clay minerals ($p > 0.05$). In comparison to the loaded clay minerals, pure CIP solution rapidly reaches an equilibrium concentration with a short half-life time of 0.2 h to a plateau of 100% cumulative release. The sustained profile of the CIP release from the clay minerals is ascribed to both CIP adsorption to the HNT surface and the antibiotic hindered out-diffusion within the HNT mesopores (Massaro et al., 2021). A variety of release profiles for CIP-loaded HNT have been

reported in the literature with half-time values ranging from 1 h to days. For example, aminosilanzed HNT loaded with 7 wt. % CIP were shown to release their antibiotic cargo into PBS (pH 7.4) within ~4 h with a half-time of 1 h (Rawtani et al., 2017). In a different report, a more sustained profile was measured for CIP-loaded HNT with a 40 % release after 12 h (Lvov et al., 2016). Moreover, HNT that were loaded with 2.6 wt. % CIP using a high-concentration methanol solution exhibited only 30 % cumulative release after 1 day at pH 7.4. It should be noted that the concentration of HNT inside the dialysis bag used for the release experiment in this work was as high as 20 mg mL⁻¹ (Massaro et al., 2021). Therefore, this wide range of profiles could be accounted for by differences in the HNT origin (Wong et al., 2021), loading conditions, as well as the release measurement technique.

To complement the CIP release studies, the exerted antibacterial activity of the released antibiotic against *E. coli* was characterized as a function of release time by the BMD method. Fig. 5c presents the attained inhibition values (normalized to the clay mineral mass) for the loaded E-HNT and HNT along with their corresponding fit of a one-phase exponential saturation model (with R square values of 0.935 and 0.989, respectively). While both clay minerals exhibit similar kinetics with a half-time of 0.3 h ($p > 0.05$), the CIP-loaded E-HNT exert a superior inhibitory effect (>25% higher) already after 1 h release ($p < 0.05$). This difference can be attributed to the higher CIP content in the E-HNT, see Fig. 3a. Characteristic bacterial growth curves used for calculating the normalized inhibition values are presented in Supporting Information, Fig. S7 for the released CIP and an equivalent fresh drug solution.

4. Conclusions

We investigate for the first time the effect of acidic etching of Halloysite nanotubes on their loading capacity of the potent antibiotic CIP. Under the optimized loading at near-physiological conditions (PBS, pH 6-7) the E-HNT hold ca. 40 % more CIP than pristine HNT (2.3 and 1.4 wt. %, respectively). According to the solid-state characterization of the loaded clay mineral, the underlying mechanism of E-HNT loading is suggested to be similar to that of pristine HNT, namely, CIP adsorption via electrostatic interactions between its zwitterionic form and the clay mineral silica surface. In addition, CIP loading onto the etched clay mineral significantly enhances the thermal stability of the antibiotic in comparison to its pure form. The sustained release profile of the loaded antibiotic is similar for HNT and E-HNT with a half time of about 0.5 h and a plateau value of 80 % cumulative release. The antibacterial activity of the CIP-loaded E-HNT was demonstrated, by two different methods (BMD and zone of inhibition) to be as potent as that of pure CIP against *E. coli*. Furthermore, after 1 h of release, the inhibitory effect of loaded E-HNT was found to be profoundly higher than that of CIP-loaded HNT. Thus, we conclude that the facile acidic etching of HNT is an effective route to further enhance their already remarkable attributes as a prominent host for antimicrobials. Moreover, the effective loading under mild near-physiological conditions, presented herein, can be applied for the design of sophisticated E-HNT-based delivery systems which integrate functional biomolecules for targeting or triggered release (Wang et al., 2021a; Prinz Setter et al., 2021; Tan et al., 2021)

Funding

This research was partially supported by the Russell Berrie Nanotechnology Institute, Technion.

CRedit authorship contribution statement

Ofer Prinz Setter: Conceptualization, Methodology, Investigation, Data curation, Writing – original draft, Writing – review & editing. **Lisa Dahan:** Investigation, Writing – original draft. **Hanan Abu Hamad:** Investigation. **Ester Segal:** Conceptualization, Methodology, Supervision, Resources, Writing – review & editing, Funding acquisition.

Declaration of Competing Interest

The authors declare that they have no known competing financial interests or personal relationships that could have appeared to influence the work reported in this paper.

Acknowledgments

We thank Prof. Sima Yaron and her lab manager Dina Shahar at the Faculty of Biotechnology and Food Engineering, Technion-Israel Institute of Technology, for generously supplying *E. coli* K-12 strain. O. P. S is grateful to the Azrieli Foundation for the award of an Azrieli Fellowship.

Appendix A. Supplementary data

Supplementary data to this article can be found online at <https://doi.org/10.1016/j.clay.2022.106629>.

References

- Abdullayev, E., Lvov, Y., 2016. Halloysites for controllable loading and release. In: Peng Yuan, A.T., Faiza, B. (Eds.), *Developments in Clay Science*. Elsevier, pp. 554–605. <https://doi.org/10.1016/B978-0-08-100293-3.00022-4>.
- Abdullayev, E., Joshi, A., Wei, W., Zhao, Y., Lvov, Y., 2012. Enlargement of Halloysite clay nanotube lumen by selective etching of aluminum oxide. *ACS Nano* 6, 7216–7226. <https://doi.org/10.1021/nn302328x>.
- Barfod, K.K., Bendtsen, K.M., Berthing, T., Koivisto, A.J., Poulsen, S.S., Segal, E., Verleysen, E., Mast, J., Hollander, A., Jensen, K.A., Hougaard, K.S., Vogel, U., Hölländer, A., Jensen, K.A., Hougaard, K.S., Vogel, U., 2020. Increased surface area of halloysite nanotubes due to surface modification predicts lung inflammation and acute phase response after pulmonary exposure in mice. *Environ. Toxicol. Pharmacol.* 73, 103266 <https://doi.org/10.1016/j.etap.2019.103266>.
- Blagojević, B., Cetojević-Simin, D., Djurić, S., Lazzara, G., Milioto, S., Agić, D., Vasile, B. S., Popović, B.M., 2022. Anthocyanins and phenolic acids from *Prunus spinosa* L. encapsulation in halloysite and maltodextrin based carriers. *Appl. Clay Sci.* 222, 106489 <https://doi.org/10.1016/J.CLAY.2022.106489>.
- Cheng, R., Li, H., Liu, Z., Du, C., 2018. Halloysite nanotubes as an effective and recyclable adsorbent for removal of low-concentration antibiotics ciprofloxacin. *Minerals* 8, 387. <https://doi.org/10.3390/min8090387>.
- Daou, I., Lecomte-Nana, G., Tessier-Doyen, N., Peyratout, C., Gonon, M., Guinebretiere, R., 2020. Probing the dehydroxylation of kaolinite and Halloysite by in situ high temperature X-ray diffraction. *Minerals* 10, 480. <https://doi.org/10.3390/min10050480>.
- Deng, L., Yuan, P., Liu, D., Du, P., Zhou, J., Wei, Y., Song, Y., Liu, Y., 2019. Effects of calcination and acid treatment on improving benzene adsorption performance of halloysite. *Appl. Clay Sci.* 181, 105240 <https://doi.org/10.1016/j.clay.2019.105240>.
- Duan, W., Wang, N., Xiao, W., Zhao, Y., Zheng, Y., 2018. Ciprofloxacin adsorption onto different micro-structured tourmaline, halloysite and biotite. *J. Mol. Liq.* 269, 874–881. <https://doi.org/10.1016/j.molliq.2018.08.051>.
- El-Gamel, N.E.A., Hawash, M.F., Fahmey, M.A., 2012. Structure characterization and spectroscopic investigation of ciprofloxacin drug. *J. Therm. Anal. Calorim.* 108, 253–262. <https://doi.org/10.1007/s10973-011-1584-8>.
- Fakhrullina, G., Khakimova, E., Akhatova, F., Lazzara, G., Parisi, F., Fakhrollin, R., 2019. Selective antimicrobial effects of Curcumin@Halloysite nanoformulation: a *Caenorhabditis elegans* Study. *ACS Appl. Mater. Interfaces* 11, 23050–23064. <https://doi.org/10.1021/acsami.9b07499>.
- Garcia-Garcia, D., Ferri, J.M., Ripoll, L., Hidalgo, M., Lopez-Martinez, J., Balart, R., 2017. Characterization of selectively etched halloysite nanotubes by acid treatment. *Appl. Surf. Sci.* 422, 616–625. <https://doi.org/10.1016/j.apsusc.2017.06.104>.
- Hanna, D.H., Saad, G.R., 2019. Encapsulation of ciprofloxacin within modified xanthan gum-chitosan based hydrogel for drug delivery. *Bioorg. Chem.* 84, 115–124.
- He, M., Xiao, H., Zhou, Y., Lu, P., 2015. Synthesis, characterization and antimicrobial activities of water-soluble amphiphilic copolymers containing ciprofloxacin and quaternary ammonium salts. *J. Mater. Chem. B* 3, 3704–3713. <https://doi.org/10.1039/c5tb00029g>.
- Huang, K., Ou, Q., Xie, Y., Chen, X., Fang, Y., Huang, C., Wang, Y., Gu, Z., Wu, J., 2019. Halloysite nanotube based scaffold for enhanced bone regeneration. *ACS Biomater. Sci. Eng.* 5, 4037–4047. <https://doi.org/10.1021/acsbomaterials.9b00277>.
- Igwegbe, C.A., Oba, S.N., Aniagor, C.O., Adeniyi, A.G., Ighalo, J.O., 2021. Adsorption of ciprofloxacin from water: a comprehensive review. *J. Ind. Eng. Chem.* 93, 57–77. <https://doi.org/10.1016/j.jiec.2020.09.023>.
- Jauković, V., Krajišnik, D., Daković, A., Damjanović, A., Krstić, J., Stojanović, J., Čalića, B., 2021. Influence of selective acid-etching on functionality of halloysite-chitosan nanocontainers for sustained drug release. *Mater. Sci. Eng. C* 123, 112029. <https://doi.org/10.1016/J.MSEC.2021.112029>.
- Jenne, E.A., 1972. Surface charge density dependency on Al₂O₃ content in imogolite. *Clay Clay Miner.* 2 (20), 101–103. <https://doi.org/10.1346/CCMN.1972.0200209>.

- Jiang, W.T., Chang, P.H., Tsai, Y., Li, Z., 2016. Halloysite nanotubes as a carrier for the uptake of selected pharmaceuticals. *Microporous Mesoporous Mater.* 220, 298–307. <https://doi.org/10.1016/j.micromeso.2015.09.011>.
- Joussein, E., 2016. Geology and mineralogy of nanosized tubular halloysite. In: Peng Yuan, A.T., Faïza, B. (Eds.), *Developments in Clay Science*. Elsevier, pp. 12–48. <https://doi.org/10.1016/B978-0-08-100293-3.00002-9>.
- Joussein, E., Petit, S., Churchman, J., Theng, B., Righi, D., Delvaux, B., 2005. Halloysite clay minerals - a review. *Clay Miner.* 40, 383–426. <https://doi.org/10.1180/0009855054040180>.
- Karewicz, A., Machowska, A., Kasprzyk, M., Ledwojick, G., 2021. Application of halloysite nanotubes in cancer therapy—a review. *Materials* 14. <https://doi.org/10.3390/MA14112943>.
- Khatoun, N., Chu, M.Q., Zhou, C.H., 2020. Nanoclay-based drug delivery systems and their therapeutic potentials. *J. Mater. Chem. B* 8, 7335–7351. <https://doi.org/10.1039/d0tb01031f>.
- Krepker, M., Shemesh, R., Poleg, Y.D., Kashi, Y., Vaxman, A., Segal, E., 2017. Active food packaging films with synergistic antimicrobial activity. *Food Control* 76, 117–126. <https://doi.org/10.1016/j.foodcont.2017.01.014>.
- Krepker, M., Zhang, C., Nitzan, N., Prinz-Setter, O., Massad-Ivanir, N., Olah, A., Baer, E., Segal, E., 2018. Antimicrobial LDPE/EVOH Layered Films Containing Carvacrol Fabricated by Multiplication Extrusion. *Polymers (Basel)* 10, 864. <https://doi.org/10.3390/polym10080864>.
- Lisuzzo, L., Cavallaro, G., Parisi, F., Milioto, S., Lazzara, G., 2019a. Colloidal stability of halloysite clay nanotubes. *Ceram. Int.* 45, 2858–2865. <https://doi.org/10.1016/j.ceramint.2018.07.289>.
- Lisuzzo, L., Cavallaro, G., Pasbakhsh, P., Milioto, S., Lazzara, G., 2019b. Why does vacuum drive to the loading of halloysite nanotubes? The key role of water confinement. *J. Colloid Interface Sci.* 547, 361–369. <https://doi.org/10.1016/j.jcis.2019.04.012>.
- Lvov, Y., Wang, W., Zhang, L., Fakhruddin, R., 2016. Halloysite Clay Nanotubes for Loading and Sustained Release of Functional Compounds. *Adv. Mater.* 28, 1227–1250. <https://doi.org/10.1002/adma.201502341>.
- Maged, A., Kharbush, S., Ismael, I.S., Bhatnagar, A., Sayed Ismael, I., Bhatnagar, A., 2020. Characterization of activated bentonite clay mineral and the mechanisms underlying its sorption for ciprofloxacin from aqueous solution. *Environ. Sci. Pollut. Res.* 27, 32980–32997. <https://doi.org/10.1007/S11356-020-09267-1>.
- Massaro, M., Lazzara, G., Milioto, S., Noto, R., Riela, S., 2017. Covalently modified halloysite clay nanotubes: synthesis, properties, biological and medical applications. *J. Mater. Chem. B* 5, 2867–2882. <https://doi.org/10.1039/c7tb00316a>.
- Massaro, M., Cavallaro, G., Colletti, C.G., D’Azzo, G., Guernelli, S., Lazzara, G., Pieraccini, S., Riela, S., 2018a. Halloysite nanotubes for efficient loading, stabilization and controlled release of insulin. *J. Colloid Interface Sci.* 524, 156–164. <https://doi.org/10.1016/j.jcis.2018.04.025>.
- Massaro, M., Colletti, C.G., Lazzara, G., Riela, S., 2018b. The use of some clay minerals as natural resources for drug carrier applications. *J. Functional Biomater.* 9, 58. <https://doi.org/10.3390/jfb9040058>.
- Massaro, M., Barone, G., Biddeci, G., Cavallaro, G., di Blasi, F., Lazzara, G., Nicotra, G., Spinella, G., Spinelli, G., Riela, S., 2019. Halloysite nanotubes-carbon dots hybrids multifunctional nanocarrier with positive cell target ability as a potential non-viral vector for oral gene therapy. *J. Colloid Interface Sci.* 552, 236–246. <https://doi.org/10.1016/j.jcis.2019.05.062>.
- Massaro, M., Borrego-Sánchez, A., Sánchez-Espejo, R., Viseras Iborra, C., Cavallaro, G., García-Villén, F., Guernelli, S., Lazzara, G., Miele, D., Sainz-Díaz, C.I., Sandri, G., Riela, S., 2021. Ciprofloxacin carrier systems based on hectorite/halloysite hybrid hydrogels for potential wound healing applications. *Appl. Clay Sci.* 215, 106310. <https://doi.org/10.1016/J.CLAY.2021.106310>.
- Memeno, C.F., Tabary, N., Mbey, J.A., Degoutin, S., Cazaux, F., Bacquet, M., Maton, M., Martel, B., Njopwouo, D., 2021. Intercalation of Ciprofloxacin in naturally occurring smectite from Bana: potentiality as drug delivery system and antimicrobial effects on *Escherichia coli* and *Staphylococcus aureus*. *J. Mater. Sci. Chem. Eng.* 09, 21–40. <https://doi.org/10.4236/msce.2021.98003>.
- Mesallati, H., Mugheirbi, N.A., Tajber, L., 2016. Two Faces of Ciprofloxacin: Investigation of Proton transfer in Solid State Transformations. *Crystal Growth Design* 16, 6574–6585. <https://doi.org/10.1021/acs.cgd.6b01283>.
- Mesallati, H., Conroy, D., Hudson, S., Tajber, L., 2017. Preparation and characterization of amorphous ciprofloxacin-amino acid salts. *Eur. J. Pharm. Biopharm.* 121, 73–89. <https://doi.org/10.1016/J.EJPB.2017.09.009>.
- Mohsen, E., El-Borady, O.M., Mohamed, M.B., Fahim, I.S., 2020. Synthesis and characterization of ciprofloxacin loaded silver nanoparticles and investigation of their antibacterial effect. *J. Radiat. Res. Appl. Sci.* 13, 416–425. <https://doi.org/10.1080/16878507.2020.1748941>.
- Moraes, J.D.D., Bertolino, S.R.A., Cuffini, S.L., Ducart, D.F., Bretzke, P.E., Leonardi, G.R., 2017. Clay minerals: Properties and applications to dermocosmetic products and perspectives of natural raw materials for therapeutic purposes—a review. *Int. J. Pharm.* 534, 213–219. <https://doi.org/10.1016/j.ijpharm.2017.10.031>.
- Pasbakhsh, P., Churchman, G.J., Keeling, J.L., 2013. Characterisation of properties of various halloysites relevant to their use as nanotubes and microfibre fillers. *Appl. Clay Sci.* 74, 47–57. <https://doi.org/10.1016/j.clay.2012.06.014>.
- Peña-Parás, L., Sánchez-Fernández, J.A., Vidaltamayo, R., 2019. Nanoclays for biomedical applications. In: *Handbook of Ecomaterials*, vol. 5, pp. 3543–3571. https://doi.org/10.1007/978-3-319-68255-6_50.
- Prinz Setter, O., Segal, E., 2020. Halloysite nanotubes - the nano-bio interface. *Nanoscale* 12, 23444–23460. <https://doi.org/10.1039/d0nr06820a>.
- Prinz Setter, O., Movsowitz, A., Goldberg, S., Segal, E., 2021. Antibody-Functionalized Halloysite Nanotubes for Targeting Bacterial Cells. *ACS Appl. Bio Mater.* 4, 4094–4104. <https://doi.org/10.1021/acsabm.0c01332>.
- Qin, Y., An, T., Cheng, H., Su, W., Meng, G., Wu, J., Guo, X., Liu, Z., 2022. Functionalized halloysite nanotubes as chlorpyrifos carriers with high adhesion and temperature response for controlling of beet armyworm. *Appl. Clay Sci.* 222, 106488. <https://doi.org/10.1016/J.CLAY.2022.106488>.
- Rawtani, D., Pandey, G., Tharmavaram, M., Pathak, P., Akkireddy, S., Agrawal, Y.K., 2017. Development of a novel ‘nanocarrier’ system based on Halloysite Nanotubes to overcome the complexation of ciprofloxacin with iron: An in vitro approach. *Appl. Clay Sci.* 150, 293–302. <https://doi.org/10.1016/j.clay.2017.10.002>.
- Ross, D.L., Riley, C.M., 1990. Aqueous solubilities of some variously substituted quinolone antimicrobials. *Int. J. Pharm.* 63, 237–250. [https://doi.org/10.1016/0378-5173\(90\)90130-V](https://doi.org/10.1016/0378-5173(90)90130-V).
- Rozhina, E., Batasheva, S., Miftakhova, R., Yan, X., Vikulina, A., Volodkin, D., Fakhruddin, R., 2021. Comparative cytotoxicity of kaolinite, halloysite, multiwalled carbon nanotubes and graphene oxide. *Appl. Clay Sci.* 205. <https://doi.org/10.1016/j.clay.2021.106041>.
- Saklar, S., Yorukoglu, A., 2015. Effect of acid leaching on Halloysite. *Physicochem. Problems Mineral Proces.* 51, 83–94.
- Santos, A.C., Ferreira, C., Veiga, F., Ribeiro, A.J., Panchal, A., Lvov, Y., Agarwal, A., 2018. Halloysite clay nanotubes for life sciences applications: from drug encapsulation to bioscaffold. *Adv. Colloid Interf. Sci.* 257, 58–70. <https://doi.org/10.1016/j.cis.2018.05.007>.
- Satish, S., Tharmavaram, M., Rawtani, D., 2019. Halloysite nanotubes as a nature’s boon for biomedical applications. *Nanobiomedicine (Rij)* 6, 1–16. <https://doi.org/10.1177/1849543519863625>.
- Stavitskaya, A., Batasheva, S., Vinokurov, V., Fakhruddin, G., Sangarov, V., Lvov, Y., Fakhruddin, R., 2019. Antimicrobial applications of Clay Nanotube-based Composites. *Nanomaterials (Basel)* 9, 708. <https://doi.org/10.3390/nano9050708>.
- Sun, P., Liu, G., Lv, D., Dong, X., Wu, J., Wang, D., 2015. Effective activation of halloysite nanotubes by piranha solution for amine modification via silane coupling chemistry. *RSC Adv.* 5, 52916–52925. <https://doi.org/10.1039/c5ra04444h>.
- Tan, C., Zheng, J., Feng, Y., Liu, M., 2021. Cell membrane-coated halloysite nanotubes for target-specific nanocarrier for cancer phototherapy. *Molecules* 26, 4483. <https://doi.org/10.3390/MOLECULES26154483>.
- Tan, D., Yuan, P., Annabi-Bergaya, F., Liu, D., Wang, L., Liu, H., He, H., 2014. Loading and in vitro release of ibuprofen in tubular halloysite. *Appl. Clay Sci.* 96, 50–55. <https://doi.org/10.1016/j.clay.2014.01.018>.
- Tharmavaram, M., Pandey, G., Rawtani, D., 2018. Surface modified halloysite nanotubes: a flexible interface for biological, environmental and catalytic applications. *Adv. Colloid Interf. Sci.* 261, 82–101. <https://doi.org/10.1016/j.cis.2018.09.001>.
- Wang, B., Han, Z., Song, B., Yu, L., Ma, Z., Xu, H., Qiao, M., 2021a. Effective drug delivery system based on hydrophobic and halloysite clay nanotubes for sustained release of doxorubicin. *Colloids Surf. A Physicochem. Eng. Asp.* 628, 127351. <https://doi.org/10.1016/j.colsurfa.2021.127351>.
- Wang, Q., Yang, M., Qi, X., Wang, J., Sun, K., Li, Z., Deng, G., 2021b. A novel graphene oxide decorated with halloysite nanotubes (HNTs/GO) composite used for the removal of levofloxacin and ciprofloxacin in a wide pH range. *New J. Chem.* 45, 18315–18326. <https://doi.org/10.1039/D1NJ03807A>.
- Wei, Y., Yuan, P., Liu, D., Losic, D., Tan, D., Chen, F., Liu, H., Zhou, J., Du, P., Song, Y., 2019. Activation of natural halloysite nanotubes by introducing lanthanum oxycarbonate nanoparticles via co-calcination for outstanding phosphate removal. *Chem. Commun.* 55, 2110–2113. <https://doi.org/10.1039/C8CC10314C>.
- Wolfson, J.S., Hooper, D.C., 1985. The fluoroquinolones: Structures, mechanisms of action and resistance, and spectra of activity in vitro. *Antimicrob. Agents Chemother.* 28, 581–586. <https://doi.org/10.1128/AAC.28.4.581>.
- Wong, L.W., Pasbakhsh, P., Arabi, A.M., Keeling, J., Tan, J.B.L., 2021. Halloysite nanotubes from various geological deposits: New insights to acid etching and their impacts on products’ characteristics. *J. Environ. Chem. Eng.* 9, 106235. <https://doi.org/10.1016/j.jece.2021.106235>.
- Xiong, C., Zhang, X., Lei, Y., Zhang, L., Shang, H., Zhang, B., Zhao, Y., 2021. One-pot synthesis of ultrafine Ni_{0.13}Co_{0.87}P nanoparticles on halloysite nanotubes as efficient catalyst for hydrogen evolution from ammonia borane. *Appl. Clay Sci.* 214, 106293. <https://doi.org/10.1016/J.CLAY.2021.106293>.
- Yang, F., Wang, A., 2022. Recent researches on antimicrobial nanocomposite and hybrid materials based on sepiolite and polygorskite. *Appl. Clay Sci.* 219, 106454. <https://doi.org/10.1016/J.CLAY.2022.106454>.
- Yang, H., Zhang, Y., Ouyang, J., 2016. Physicochemical properties of halloysite. In: Peng Yuan, A.T., Faïza, B. (Eds.), *Developments in Clay Science*. Elsevier, pp. 67–91. <https://doi.org/10.1016/B978-0-08-100293-3.00004-2>.
- Yuan, P., Southon, P.D., Liu, Z., Green, M.E.R., Hook, J.M., Antill, S.J., Kepert, C.J., 2008. Functionalization of Halloysite Clay Nanotubes by Grafting with γ -Aminopropyltriethoxysilane. *J. Phys. Chem. C* 112, 15742–15751. <https://doi.org/10.1021/jp805657t>.
- Zhao, M., Liu, P., 2008. Adsorption behavior of methylene blue on halloysite nanotubes. *Microporous Mesoporous Mater.* 112, 419–424. <https://doi.org/10.1016/j.micromeso.2007.10.018>.
- Zhao, Q., Liu, C., Liu, J., Zhang, Y., 2015. Development of a novel polyethersulfone ultrafiltration membrane with antibacterial activity and high flux containing halloysite nanotubes loaded with lysozyme. *RSC Adv.* 5, 38646–38653. <https://doi.org/10.1039/c5ra05062f>.
- Zhao, Y., Kong, W., Jin, Z., Fu, Y., Wang, W., Zhang, Y., Liu, J., Zhang, B., 2018. Storing solar energy within Ag-Paraffin@Halloysite microspheres as a novel self-heating catalyst. *Appl. Energy* 222, 180–188. <https://doi.org/10.1016/J.APENENERGY.2018.04.013>.